Theoretical and Applied Fracture Mechanics 125 (2023) 103931

Contents lists available at ScienceDirect

Theoretical and Applied Fracture Mechanics

journal homepage: www.elsevier.com/locate/tafmec

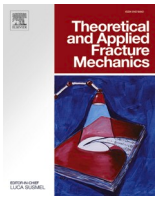

# Effects of temperature on tensile and fracture performance of Ti6Al4V alloy fabricated by laser powder bed fusion

Yingmeng Xiao [a,b], Guian Qian [a,b,*], Jingyu Sun [a,b], Filippo Berto [c], Jose A.F. Correia [d], Youshi Hong [a,b]

[a] State Key Laboratory of Nonlinear Mechanics (LNM), Institute of Mechanics, Chinese Academy of Sciences, Beijing 100190, China
[b] School of Engineering Science, University of Chinese Academy of Sciences, Beijing 100049, China
[c] Department of Mechanical and Industrial Engineering, Norwegian University of Science and Technology (NTNU), Richard Birkelands vei 2b, 7491 Trondheim, Norway
[d] Construt and Faculty of Engineering, University of Porto, Porto 4200-465, Portugal

ARTICLE INFO

*Keywords:*
Ti6Al4V alloy
Temperature effect
Fracture property
Tensile strength
Laser powder bed fusion

ABSTRACT

Research on low temperature resistance and fracture behavior of additively manufactured (AMed) titanium alloy is lacking. In this study, both tensile and fracture behavior of Ti6Al4V alloy produced by laser powder bed fusion (LPBF) were investigated at four temperatures (293, 223, 173, 123 K). Microscopic observation and finite element analysis were used to study the fracture mechanism. A correlation of fracture toughness and temperature between 123 and 293 K was obtained. As the temperature decreases, the fracture mode of the specimen changes from ductile fracture to a mixed mode of ductile and brittle fracture, the tensile strength increases and the fracture toughness decreases. These differences could be interpreted by the crack tip plastic zone (CTPZ) and microscopic plastic deformation. Compared to the wrought Ti6Al4V alloy, the fracture originations are mainly from LPBF defects, i.e., lack of fusion (LOF) defects and gas pores.

## 1. Introduction

Additive manufacturing (AM) is an advanced manufacturing technology that is capable of fabricating complex and near-net shape components directly from raw materials [1–3]. AM is based on a novel material incremental manufacturing philosophy as opposed to traditional subtractive manufacturing. Laser powder bed fusion (LPBF) is one of the most promising AM techniques due to the minimal post-processing machining required in the final application, and has been widely used for complex and customized parts made of metallic materials, particularly the Ti6Al4V, AlSi10Mg and Inconel 718 alloys [4,5]. A large number of studies have been conducted to establish profound processing-microstructure-mechanical performance relationships of LPBF objects by surveying the processing parameter windows [6–8], performing various heat treatments [9], and conducting various mechanical tests [10,11]. However, it is very important to study the fracture property because the fracture toughness ultimately defines the cracking resistance of materials and determines the structural integrity of engineering parts. In recent years, ensuring the structural integrity and reliability of engineering components produced for quality assessment and certification purposes is still a major challenge that impends the widespread adoption of AM technology [12]. Keeping this in view, it is necessary to research the fracture behavior of LPBF metals.

The α + β biphasic structure alloy Ti6Al4V is currently the most extensively used titanium alloy due to its combination of high specific strength, toughness and fatigue resistance along with good heat resistance and cryogenic embrittlement resistance [13]. It is popular in high performance applications, such as aerospace, marine, cryogenic and elevated temperature structural components. However, the inherent physical and mechanical properties of Ti6Al4V titanium alloy will introduce severe work hardening, which limits its wide application. LPBF perfectly overcomes the machining challenge of titanium alloy due to the following characteristics: i) the integration of design, manufacturing and material; ii) flexibility in terms of manufacturing arbitrary configurations of components [12,14]. During the LPBF process, the short interactions, high temperature gradients and fast solidification rate endow the Ti6Al4V alloy with more complex micro- and meso-structures: prior β grains (PBGs), colonies, laths and intermetallic phase [15,16]. Primary grains tend to extend across an entire prior β grain (PBG), and the secondary, tertiary and quartic $\alpha'$ martensite

* Corresponding author at: State Key Laboratory of Nonlinear Mechanics (LNM), Institute of Mechanics, Chinese Academy of Sciences, Beijing 100190, China.
*E-mail address:* qianguian@imech.ac.cn (G. Qian).

https://doi.org/10.1016/j.tafmec.2023.103931
Received 11 March 2023; Received in revised form 7 May 2023; Accepted 9 May 2023
Available online 18 May 2023

within columnar prior β grains result in a basket weave structure [17]. These structures have a great influence on the tensile property, mode I plane strain fracture toughness ($K_{IC}$), fatigue crack growth rate, and unnotched fatigue strength.

In general, the yield strength and ultimate tensile strength of the LPBF Ti6Al4V alloy can meet or even exceed those of conventional fabrication, while the ductility of LPBF Ti6Al4V is generally lower than that of forged and cast Ti6Al4V alloys [18,19]. Fatigue crack growth rate $\Delta K_{th}$ for heat treated LPBF Ti6Al4V reported in the literature is similar to that of the wrought material (3.1 ~ 4.6 MPa $\sqrt{m}$), except that the high cycle fatigue strength (ranging from 200 ~ 350 MPa) is significantly inferior to that of the wrought alloy (450 ~ 650 MPa) [20]. Excessive presence of defects, such as pores and lack of fusion (LOF), has been associated with poor fatigue performance in certain studies. This can result in either internal or surface cracking [21]. The value of $K_{IC}$ of the as-built LPBF Ti6Al4V alloys is typically only between 16 and 28 MPa $\sqrt{m}$, owing to the presence of inherent defects and residual stress [22]. This value is much lower than that of the wrought produced Ti6Al4V alloys, which ranges from 30 to 80 MPa $\sqrt{m}$ depending on the specific microstructure [20,23]. After improving the process parameters and applying heat treatment, the $K_{IC}$ of LPBF Ti6Al4V alloys can increase to 48 ~ 58 MPa $\sqrt{m}$ [16]. Furthermore, duplex heat treatment can significantly improve the $K_{IC}$, with values ranging from 77 ~ 106 MPa $\sqrt{m}$ due to coarser α laths and preservation of the prior β mesostructure [24]. LPBF Ti6Al4V alloy printings with large-scale configuration have been used for heavy and often permanent structural components, with the challenge of tending to fracture [25].

The mechanical behavior of titanium and its alloys at cryogenic temperatures has been extensively studied. However, the applicability of Ti6Al4V alloy has been limited to 77 K due to its low cryogenic fracture toughness, which is insufficient for temperatures below 77 K [26]. Yuri *et al.* [27] discovered that the fatigue strength of notched specimens is lower at 4 K than at 77 K, primarily because of the increased notch sensitivity at lower temperatures. Singh *et al.* [28] investigated the plastic deformation and tensile strength of Ti6Al4V alloyed with minor additions of Boron at cryogenic temperatures, and the yield strength variation at different temperatures shows that the colony size determines the yield strength of the alloy at 77 K, implying that dislocation-mediated plasticity dominates above 77 K, while twinning dominates the flow response at 20 K. Up to now, it is clear that there is a lack of studies on the tensile and fracture behavior of LPBF Ti6Al4V parts at low temperatures. Considering the wide application of LPBF Ti6Al4V titanium alloy in aerospace and space exploration, it is of great interest to investigate the temperature dependence of the tensile and fracture properties.

This paper aims to investigate the effect of temperature on the uniaxial tensile and fracture behavior of LPBF Ti6Al4V alloys. A series of quasi-static tensile tests and fracture toughness experiments were conducted at different temperatures. The initial microstructure was characterized using the electron backscatter diffraction (EBSD) analysis. The fracture surfaces were observed by scanning electron microscopy (SEM) and the fracture mechanisms of the material were discussed. In addition, finite element (FE) simulation was used to calculate the size of the crack tip plastic zone (CTPZ), which is the area of local plastic deformation of the material presented near the crack tip. It is caused by stress concentrations that may be due to cracks, defects, etc. It has been reported that the CTPZ has an important influence on the fracture behavior of the material [29]. Finally, the correlation of CTPZ volume with load at different temperatures was obtained.

## 2. Specimen preparation and test procedure

### 2.1. Material and LPBF process procedure

In order to perform the tensile and fracture toughness tests, the original cylindrical and rectangular blocks were printed from pre-alloyed gas-atomized Ti6Al4V powder using the same processing parameters on a commercial EOS M290 laser powder bed fusion system in Xi'an. The Ti6Al4V powder particles used here were ranged from 15 to 53 μm in diameter and have a normal powder size distribution (PSD) with 50% of the particles smaller than 45 μm. Due to the high reactivity of the titanium alloy, the printing process was performed in an inert Argon atmosphere with a purity of 99.99%. The chemical composition of the material has been tested and is listed in Table 1. The LPBF parameters used in this study were: laser power ($P$) of 330 W, hatch spacing ($h$) of 0.09 mm, scanning speed ($v$) of 2000 mm/s, and layer thickness ($t$) of 0.03 mm, as shown in Table 2. The final input laser energy density ($E$) is 60.3 J/mm$^3$, which is calculated by the following equation [15].

$$E = \frac{P}{v \cdot h \cdot t} \tag{1}$$

The bidirectional laser beam scanning strategy adopted is "cross-hatching", as shown in Fig. 1(a). According to [30], the "cross-hatching" scanning strategy makes the entire laser energy input more balanced throughout the whole layers, which effectively prevents defect accumulation and propagation. The substrate is preheated to 35 °C to reduce the effect on the microstructure of the heat affected zone. Later, the object is created by selectively solidifying of the deposited metal powder layers with a laser beam. After the first layer is printed, the substrate is dropped one layer and the laser beam is rotated 90° to melt the powder newly spread on the surface of the object. The above process is repeated until the object is fully formed.

The round rods with a diameter of 12 mm and a length of 68 mm and the sample blocks of 72 × 32 × 33 mm$^3$ were printed along the vertical direction on the build platform, also known as 90° printing, as shown in Fig. 1(b). The coordinate system TD, RD, and AD in Fig. 1 refer to the tangential direction, radial direction, and axial direction, respectively. The axial direction corresponds to the build direction (BD). After LPBF but prior to tensile and fracture specimen machining, the printed original cylindrical and rectangular blocks were first annealed at 800 °C for 4 hours and then cooled in an Argon atmosphere to relieve the residual stresses produced in the LPBF process. The Archimedes method was used to determine the relative densities of the test specimens and the test result is 99.33%.

### 2.2. Specimens and mechanical tests

Electron backscattering diffraction (EBSD) and optical microscopy (OM) were used to characterize the initial microstructure of the LPBF Ti6Al4V alloy. The samples observed were mechanically ground with SiC sandpaper (320–5000 particle size) and polished with 0.05 μm Silica suspension ($SiO_2$ and $H_2O_2$). The grain structure was characterized by EBSD technique in a scanning electron microscope (ZEISS SIGMA 300). The scanning step was 0.5 μm and the scanning area was 300 × 400 μm$^2$. Then, HKL Channel 5 software was used for microstructure data analysis. The polished samples were etched with Kroll reagent (100 mL distilled water, 5 mL Nitric acid, and 2 mL HF) for about 10 s, and examined with an Olympus BX51 optical microscope (OM) for metallographic analysis.

Tensile tests were conducted to obtain the mechanical properties of the material for fracture toughness test and FE analysis. According to GB/T 228–2010, standard dog bone specimens with a gauge length of 27 mm and diameter of 5 mm were designed, as shown in Fig. 2(a). The loading axis was parallel to the BD at a tensile rate of 1.5 mm/min at four temperatures (293, 223, 173, 123 K). Tensile tests were performed using a microcomputer-controlled LD26.105 electronic universal testing machine, with an electronic extensometer attached to the specimen to monitor the deformation of the gauge section. The axial strain was automatically calculated by the computer based on the dimensions of the tensile specimen. Due to the limitations of the test equipment, the lowest test temperature was set at 123 K.

**Table 1**
Nominal chemical compositions of the Ti6Al4V alloy powders (wt.%).

| Element | Ti | Al | V | Fe | O | C | N | H |
|---|---|---|---|---|---|---|---|---|
| wt.% | Bal. | 6.14 | 4.01 | 0.17 | 0.11 | 0.015 | 0.0035 | 0.0021 |

**Table 2**
LPBF processing parameters of the tested specimens.

| Powder size [mm] | Laser power [W] | Scanning speed [mm/s] | Scanning space [mm] | Layer thickness [mm] | Preheating temperature [°C] | Relative density [%] | Scanning strategy |
|---|---|---|---|---|---|---|---|
| 0.015–0.053 | 330 | 2000 | 0.09 | 0.03 | 35 | 99.33 | cross-hatching |

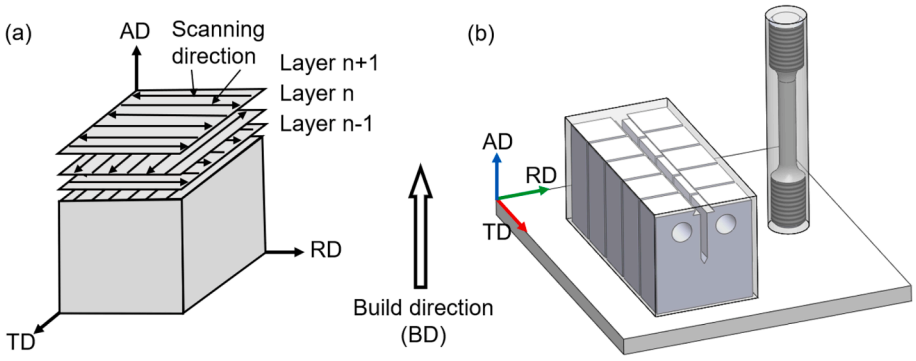


**Fig. 1.** Schematic representation of (a) the "cross-hatching" laser scanning strategy, (b) the orientation of the tensile and fracture specimens relative to the build direction.

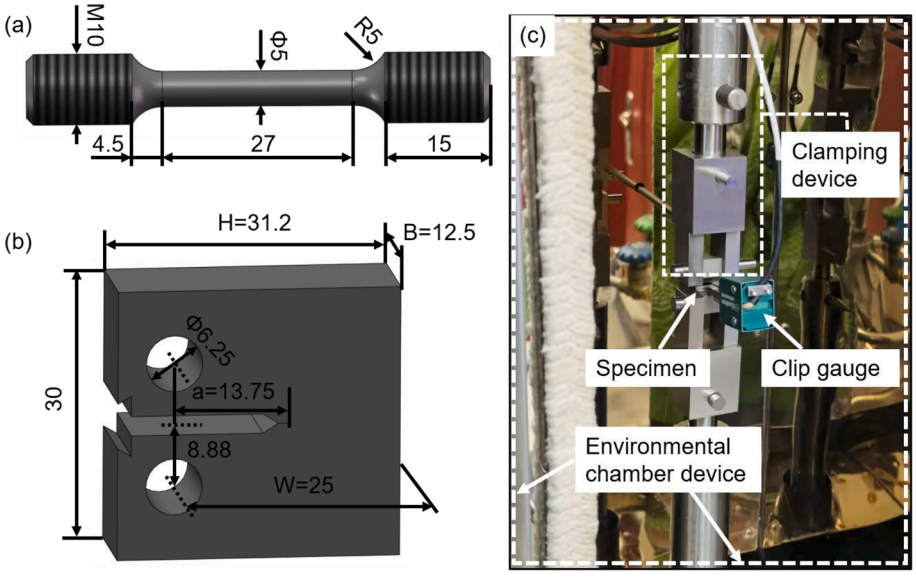


**Fig. 2.** Geometry and schematic description of (a) the tensile specimen, (b) the standard 1/2 T specimen (dimension in mm), (c) fracture toughness test setup.

Fig. 2(b) shows the 1/2 compact tension (CT) specimen (1/2 T) designed according to ASTM E399-20 for the determination of $K_{IC}$ [31]. Fatigue pre-cracking was performed on an electrohydraulic servo fatigue testing machine (EHF-EV01KZ-040-1A), and the crack length ratio ($a/W$) of all specimens was 0.55 ($a$ - crack length, $W$ - width of the specimen). The load stress intensity range $\Delta K$ was 10 ~ 15 MPa$\sqrt{m}$ in a sinusoidal waveform at a frequency of 10 Hz, and the load ratio $R$ was constant at 0.1. A clip gauge (Epsilon, 3541C-006 M-040 M-LT) attached to the specimen was used to obtain the crack mouth opening displacement (CMOD). Tensile load was applied to the 1/2 T specimen via two load pins inserted into the loading holes, and the WANCE TSE-104C-TS tensile testing machine automatically recorded the applied load using a force sensor. Liquid nitrogen spray was used for cooling, and the test was conducted in the environmental chamber device (WANCE, GD200A), as shown in Fig. 2(c). Prior to loading, the specimen was kept at the corresponding test temperature for at least 30 min. Then, the specimens were fractured at a loading rate of 0.2 mm/min. Finally, the fracture surfaces of the tensile and fracture specimens were observed by tungsten filament scanning electron microscopy (SEM, JSM-IT300). The surface roughness of all specimens was characterized by Ra according to GB/T131-2006. Ra is the arithmetic mean height of the profile lines. The surface of the tensile specimens was polished to Ra 0.8. The main surface

of the 1/2 T specimens was polished to Ra 0.4, and the surface of the two loading holes was polished to Ra 0.2. The experiment and specimen matrix are listed in Table 3.

### 2.3. Crack tip plasticity and finite element modeling

#### 2.3.1. Crack tip plasticity

The Mode I crack-tip plastic zone shapes estimated from the Irwin's approach and the von Mises yield criterion gives the following formulas [32]

$$r_y(\theta) = \frac{1}{4\pi}\left(\frac{K_I}{\sigma_{YS}}\right)^2\left[1+\cos\theta+\frac{3}{2}\sin^2\theta\right] \text{ for plane stress} \tag{2}$$

$$r_y(\theta) = \frac{1}{4\pi}\left(\frac{K_I}{\sigma_{YS}}\right)^2\left[(1-2\nu)^2(1+\cos\theta)+\frac{3}{2}\sin^2\theta\right] \text{ for plane strain} \tag{3}$$

where $K_I$ is the stress intensity factor which is used to characterize the linear elastic stress field at the crack tip [33], $\theta$ is the angle with the crack plane in polar coordinates, $\nu$ is Poisson's ratio. However, Eqs. (2) and (3) are not strictly correct in this case because they are based on a purely linear elastic analysis.

Rice [29] proposed a fracture parameter of $J$-integral and showed that for deformation plasticity (nonlinear elasticity), the value of $J$-integral is independent of the integration path around the crack. Using the concept of $J$-integral, Hutchinson [34] and Rice and Rosengren [35] independently evaluated the character of crack tip fields in a nonlinear elastic power-law hardening material. When elastic strains are included, the relationship between plastic strain and stress for uniaxial deformation is given by

$$\varepsilon = \frac{\sigma}{E} + \alpha\frac{\sigma_0}{E}\left(\frac{\sigma}{\sigma_0}\right)^n \tag{4}$$

where $\sigma_0$ is the reference stress value, usually equal to the yield strength of the material, $E$ is the Young's modulus, $\alpha$ is a dimensionless constant, and $n$ is the strain-hardening exponent. Eq. (4) is known as the Ramberg-Osgood equation, and is widely used for curve-fitting of true stress–strain data. Hutchinson obtained the following asymptotic variation of stress and strain ahead of the crack tip

$$\begin{aligned}\sigma_{ij} &= \sigma_0\left(\frac{J}{\alpha\sigma_0\varepsilon_0 I_n r}\right)^{\frac{1}{n+1}}\tilde{\sigma}_{ij}(n,\theta) \quad (a)\\ \varepsilon_{ij} &= \alpha\varepsilon_0 r\left(\frac{J}{\alpha\sigma_0\varepsilon_0 I_n r}\right)^{\frac{n}{n+1}}\tilde{\varepsilon}_{ij}(n,\theta) \quad (b)\end{aligned} \tag{5}$$

where $\varepsilon_0 = \varepsilon_0/E$, $I_n$ is an integration constant that depends on $n$, $\tilde{\sigma}_{ij}$ and $\tilde{\varepsilon}_{ij}$ are the dimensionless functions of $n$ and $\theta$. Rice and Rosengren obtained essentially identical results to Hutchinson's solutions for plane strain in a different format. Eq. (5) is therefore referred to as the HRR field, and the $J$-integral is used to describe the singularity intensity of the crack-tip stress field for elastic–plastic hardening materials [36].

In fact, most metallic materials have a plastic zone at the crack tip before and during fracture, and the crack is also blunted by plastic deformation. Therefore, within a small local area, plastic yielding will make the theoretical results based on the linear elastic response unable to describe the stress and strain behavior in this local area. The effect of the small-scale yielding (SSY) theory considering the plastic zone is discussed in detail for corrections based on the linear elastic fracture mechanics [37]. By considering the stress relaxation caused by plastic deformation, the plastic zone in the crack tip is approximated as

$$r_p = \frac{1}{\pi}\left(\frac{K_I}{\sigma_{YS}}\right)^2 \text{ for plane stress} \tag{6}$$

$$r_p = \frac{(1-2\nu)^2}{\pi}\left(\frac{K_I}{\sigma_{YS}}\right)^2 \text{ for plane strain} \tag{7}$$

In the case of SSY conditions (CTPZ is very small relative to the characteristic length $L$, e.g., crack size, $a$), both $K_I$ and $J$-integral characterize the crack tip conditions [32]. At a short distance from the crack tip, defined as $r_k$ ($r_k \approx 0.3a \sim 0.5a$), the stress is proportional to $1/\sqrt{r}$. By assuming monotonic, quasi-static loading, a $J$-dominated region occurs in the plastic zone $r_p$ ($r_p \ll r_k$, at least one order of magnitude), where the elastic singularity no longer applies. Well within the plastic zone, the HRR solution is approximately valid and stresses vary as $r^{-1/(n+1)}$. The finite strain region occurs within the plastic zone $r_p$ about $2\delta$ ($\delta$ is the crack tip opening displacement proposed by Wells [38]) of the crack tip, where large deformations invalidate the HRR theory. In summary, for SSY theory, $K_I$ uniquely characterizes the crack tip conditions, although the $1/\sqrt{r}$ singularity does not exist all the way to the crack tip, and the typical $K_I$-dominated region is $r_p < r \ll r_k$; Similarly, the $J$-integral uniquely characterizes the crack-tip conditions, although the deformation plasticity and small strain assumptions are invalid in the finite strain regime. Under SSY conditions, the $J$-integral is related to the $K_I$ as

$$J = \frac{(1-\nu^2)K_I^2}{E} \tag{8}$$

Therefore, we used the elastic–plastic $J$-integral to characterize the crack tip filed and to obtain the CTPZ in the SSY condition instead of correcting the linear elastic fracture mechanics $K_I$ in this study.

#### 2.3.2. Finite element modeling

FE analysis was used to evaluate the effects of CTPZ on the fracture toughness of 1/2 T specimens tested at different temperatures based on the contour integral using the commercial FE analysis software ABAQUS. The complex microstructure of the LPBF Ti6Al4V alloy was ignored, and the anisotropy was not considered. Since the specimens were heat treated, the material property of LPBF Ti6Al4V was assumed as isotropic and elastoplastic, and the Poisson's ratio $\nu = 0.34$ and Young's modulus were given in Table 4. The true stress–strain curves were used to consider the plastic property of the material in this study, as shown in Fig. 6. Taking advantage of geometric symmetry, one quarter of the 1/2 T specimen was modeled. On the fracture surface ($YOZ$ ($x = 0$) plane), the $X$-axis symmetry constraint ($U_x = UR_y = UR_z = 0$) was set; on the mid-symmetry surface ($XOY$ ($z = 0$) plane) of the specimen, the $Z$-axis symmetry constraint ($U_z = UR_y = UR_x = 0$) was used as shown in Fig. 3(a).

The boundary conditions used in the finite element calculation are important to ensure that the deformation response is consistent with the macroscopic mechanical behavior of the material. In a three-dimensional fatigue crack propagation simulation, it is shown that the horizontal displacement constraints in all boundary conditions are in better agreement with the analytical results than applying the load to the reference point coupled to the loading region [39]. For convergence and accuracy considerations, the horizontal displacement constraint of 0.3 mm was applied to a rigid pin in contact (frictionless) with the specimen instead of applying loads in this study. The element type used was a 20-node quadratic hexahedral reduced integration element (C3D20R brick element). Considering the influence of stress singularity, the brick element was converted to a 15-node quadratic triangular prism element (C3D15 wedge element) at the crack tip of the specimen, thus avoiding the use of additional singularity elements in the finite element

**Table 3**
Summary of different experiment types and number of specimens with respect to the test temperatures in each case.

| Test temperatures [K] | | 293 | 223 | 173 | 123 |
|---|---|---|---|---|---|
| Experiment type | Specimen type | Test number | | | |
| Monotonic tensile | Tensile specimen | 3 | 2 | 2 | 2 |
| Fracture test | 1/2 T specimen | 4 | 3 | 3 | 3 |

**Table 4**
Tensile property of LPBF Ti6Al4V alloy at different test temperatures. Properties of wrought Ti6Al4V alloys at different temperatures are taken from [28] and [44].

| Manufacturing Technology | Temp. [K] | $\sigma_{YS}$ [MPa] | $\sigma_{UTS}$ [MPa] | $E$ [GPa] | $\varepsilon_f$ [%] | $n$ [/] |
|---|---|---|---|---|---|---|
| LPBF | 293 | 973 ± 9 | 1027 ± 2 | 112.5 ± 2.40 | 15.95 ± 0.10 | 18.33 |
| | 223 | 1092 ± 5 | 1133 ± 3 | 116.4 ± 1.57 | 15.56 ± 0.53 | 12.94 |
| | 173 | 1187 ± 20 | 1222 ± 15 | 124.0 ± 0.80 | 13.65 ± 0.18 | 21.19 |
| | 123 | 1314 ± 4 | 1332 ± 3 | 118.3 ± 2.52 | 13.04 ± 3.30 | 25.97 |
| wrought [28] | 298 | 784.8 ± 13.4 | 830.6 ± 23.3 | / | 13.2 ± 2.4 | / |
| | 77 | 1237.5 ± 7.5 | 1353.5 ± 4.5 | / | 2.9 ± 1.2 | / |
| | 20 | 1386 ± 27 | 1544.5 + 1.5 | / | 5.85 ± 1.4 | / |
| wrought [44] | 293 | 859 | 908 | 111.7 | 13.6 | / |
| | 77 | 1344 | 1392 | 128.6 | 12.1 | / |

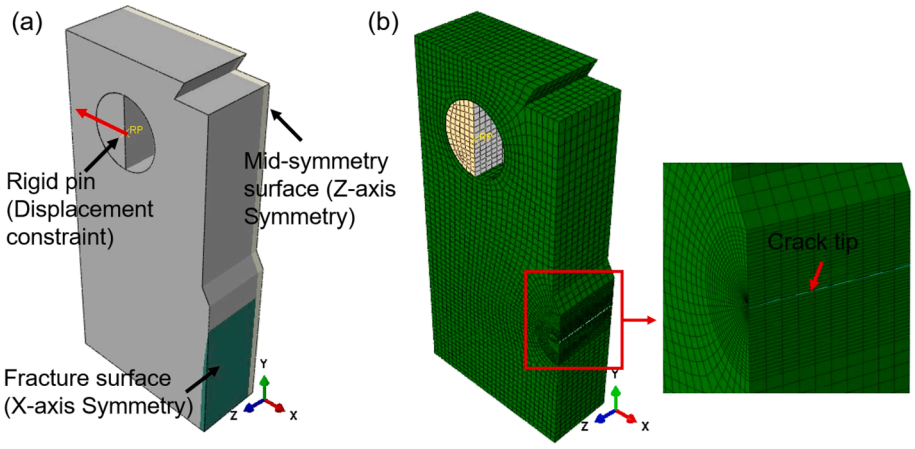


**Fig. 3.** (a) Boundary conditions and (b) crack tip mesh details of the 3D 1/2 T specimen.

simulation. Due to the severe plastic deformation in the crack tip region, a refined mesh was performed to improve the calculation accuracy as shown in Fig. 3 (b). The number of elements in the model was 23080 and the $J$-integral was calculated using the ABAQUS procedure.

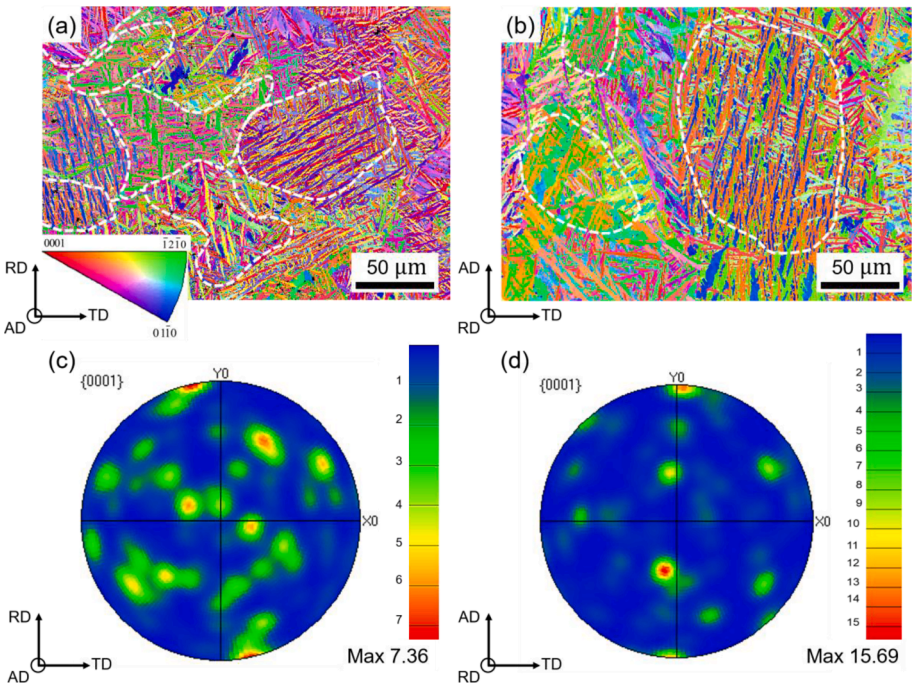


**Fig. 4.** Initial microstructure of the LPBF Ti6Al4V alloy: EBSD inverse pole figure map in the TD-RD plane (a) and the TD-AD plane (b), the {0001} pole figure of the TD-RD plane (c) and the TD-AD plane (d). The white dashed lines in (a) and (b) represent prior β grain boundaries.

## 3. Results and discussion

### 3.1. Microstructure

Fig. 4(a-b) shows the EBSD inverse pole figure (IPF) map of the TD-RD plane perpendicular to the BD, and the TD-AD plane parallel to the BD. It can be seen that the initial microstructure of the tested sample is composed of a large number of prior β grains (PBGs), colonies, and laths. In LPBF processing, the high cooling rate and temperature gradient provide a sufficient driving force for the formation of laths with almost all the possible variants [24]. At medium temperatures (800 °C), the primary $\alpha' \rightarrow \alpha$ transformed grains become dominant, while the prior β grains remain unchanged [9]. Additionally, the relatively rapid cooling resulting from the single-step cooling process leads to the formation of the basket weave structure frequently observed in LPBF Ti6Al4V alloy [17]. It is apparent that the material predominantly consists of a lamellar α structure, as evidenced by needle-shaped α laths within the β grains.

The maximum peak intensity, which is also known as texture strength of the {0001} pole figure (PF) of the TD-RD plane and the TD-AD plane are 7.36 and 15.69 respectively, as shown in Fig. 4(c-d). With almost the same number of variants, the texture strength differs by almost 50%, indicating that there are more laths with similar orientations in the TD-RD plane. It is unlikely that the anisotropy can be completely eliminated by stress relieving annealing. It is expected that microstructure anisotropy has significant effect on mechanical properties such as the tensile strength, high-cycle and very-high-cycle fatigue properties, and crack growth rate [40,41]. The columnar PBGs structure may be responsible for the anisotropy observed in the LPBF Ti6Al4V alloy [42]. The heat treatment process significantly affects the texture of LPBF Ti6Al4V, which in turn affects the mechanical properties. Overall, the proper heat treatment not only mitigates the anisotropy in properties, but also improves the ductility, fracture toughness, and fatigue crack growth resistance [24].

Fig. 5 shows the optical microscopy images of the LPBF Ti6Al4V alloy. The prior β grains in the TD-RD plane show a checkerboard pattern and the average grain length is about 90 μm, which is the same as the laser scanning space, as shown in Fig. 5(a). The microstructure of the TD-AD plane in Fig. 5(b) shows the vertical columnar prior β grains which are aligned along the BD. These grains are discontinuous due to the mismatch between the successive laser tracks. Kumar *et al.* [16] argued that due to the existence of the melt pool boundaries (MPBs), columnar grains in the TD-AD plane become shorter and grain size becomes smaller. In addition, only a small number of defects were observed in the LPBF Ti6Al4V alloy compared to the as-built Ti6Al4V alloy [43], indicating that heat treatment can effectively reduce the porosity and improve the relative density.

### 3.2. Tensile property

#### 3.2.1. Stress-strain curves

Fig. 6 displays the true stress–strain curves for the LPBF Ti6Al4V specimens at various temperatures. The 0.2% offset yield strength $\sigma_{YS}$, ultimate tensile strength $\sigma_{UTS}$, and elongation $\varepsilon_f$ are summarized in Table 4. At room temperature (293 or 298 K), the $\sigma_{YS}$, $\sigma_{UTS}$ and $\varepsilon_f$ of the LPBF specimen are slightly higher than those of the wrought Ti6Al4V alloys. It is clear that the temperature has a significant effect on the tensile strength and elongation, as shown in Fig. 7. For the LPBF Ti6Al4V alloy, both $\sigma_{YS}$ and $\sigma_{UTS}$ decrease with increasing temperature, while $\varepsilon_f$ increases with increasing temperature at 123–293 K. While for the wrought Ti6Al4V alloys, the $\varepsilon_f$ at 20 K is higher than that at 77 K. This is because that the plastic deformation of the Ti6Al4V alloy changes from slip to twinning-dominated flow when the temperature is lowered from room temperature [37]. Overall, the effect of temperature on the tensile properties of the LPBF Ti6Al4V alloy is similar to that of the conventional wrought Ti6Al4V alloys at 77–293 K. That is, the tensile strength increases and the elongation decreases with decreasing temperature [28,44], as shown in Table 4. The $\sigma_{YS}$ at 293 K is 341 MPa higher than that of the specimen at 123 K. The Young's modulus increases gradually with the decreasing of temperature, but the Young's modulus of the specimen at 123 K is lower than that at 173 K. Considering the number of specimens and the accuracy of test, more experiments are still needed to investigate the relationship between temperature and Young's modulus. Overall, $\sigma_{UTS}$ is not much higher than $\sigma_{YS}$ at the same temperature. This may be related to the low work- hardening capability of the LPBF

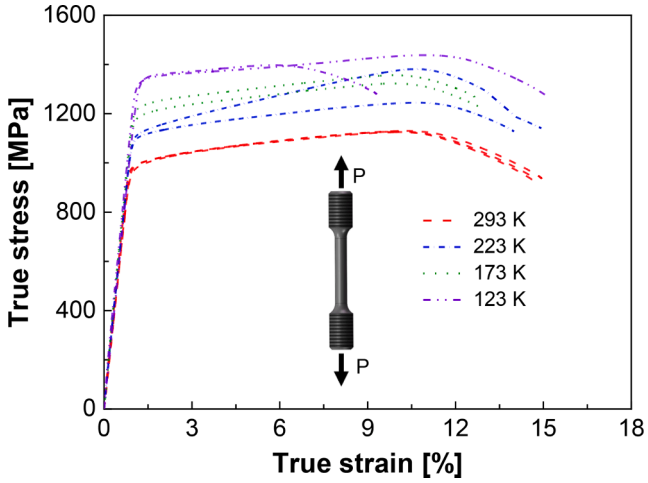


**Fig. 6.** True stress–strain curves of LPBF Ti6Al4V alloy.

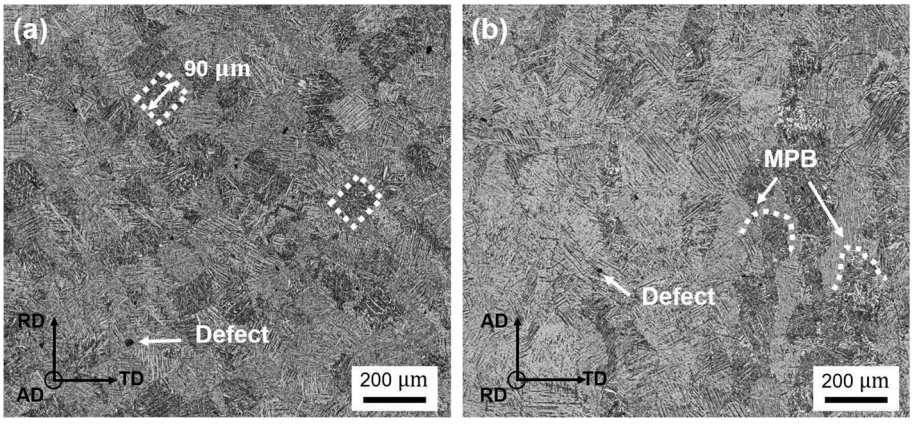


**Fig. 5.** Optical microscopy images of the LPBF Ti6Al4V alloy: (a) TD-RD plane, (b) TD-AD plane.

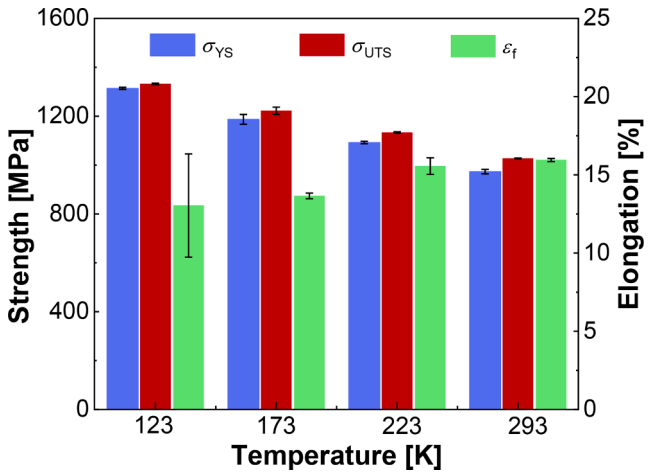


**Fig. 7.** Comparison of tensile strength and fracture elongation at different temperatures.

Ti6Al4V alloy, since all the $n$ at different temperatures are greater than 12 in Table 4. In addition, since the elongation of Ti6Al4V alloy is mainly determined by the powder size and porosity, the elongation of the same powder batch does not change significantly with the test temperature [6,12].

#### 3.2.2. Tensile fracture morphology

The fracture surfaces after tensile testing of the LPBF Ti6Al4V specimens are shown in Fig. 8. A cup-cone shape of the necking region consisting of shear lips at the periphery is observed in Fig. 8(a), indicating the ductile fracture mode at room temperature. The central fibrous region in the fracture surface is the plane strain part of the unstable propagation of the tensile crack. Many fine and coarse deep equiaxed dimples are distributed in the fibrous zone of the fracture surface (Fig. 8(b, d)), which is the result of the nucleation, growth, and subsequent coalescence of the voids during the tensile loading driven by the hydrostatic tension in the neck [45]. Micro-void coalescence is the dominant fracture mechanism in the LPBF Ti6Al4V alloy with the fine microstructure [46]. At room temperature (~ 293 K), some researchers found that the LPBF Ti6Al4V alloy exhibits a combination of ductile and brittle fracture [40], while some researchers suggested that there are different fracture mechanisms exist for coarse powder specimens and fine powder specimens, the former being ductile and the latter brittle [45]. Additionally, the microstructure and defect distribution of AM materials are influenced by several processing parameters such as powder size, distribution, laser energy, and scanning spacing. Therefore, the factors affecting the mechanical properties of LPBF materials are complex and interrelated.

The specimens at low temperatures have no clear evidence of necking and the fracture surface is not central symmetrical with a mixed mode of ductile and brittle fracture, as shown in Fig. 8(c, e, g). The fracture initiation (indicated by the red arrows) may be due to the close interaction between the defect and the fracture surface. The shear lip surrounding the central fiber region is the plane stress part, it is discontinuous and characterized by an extension from the onset of fracture region in the edge to the central flat region. The lower the temperature, the more obvious the discontinuity of the shear lip. Small elongated dimples and quasi-cleavage fracture features can be seen on these fracture surfaces (Fig. 8(f, h)). The elongated dimples, discontinuous shear lip, and cleavage-like facets suggest that the fracture is complex and involves a ductile–brittle mechanism [19]. Some large defects can be found in the interior of the fracture surface, i.e., "plateau" or "basin" (indicated by the black arrows) [45]. The difference in the fracture mechanism of the specimens at different temperatures may be due to the different defect and dislocation motion. It is well known that metals generally rely on dislocation motion to coordinate deformation. As the temperature decreases, the dislocation motion slows down. Since there is not enough plasticity to induce fracture, a mixed mode of ductile–brittle fracture is formed [47].

### 3.3. Fracture toughness

#### 3.3.1. Temperature effect on fracture properties

According to ASTM E399-20, the Mode I provisional fracture toughness $K_Q$ is obtained from the following equation

$$K_Q = \frac{P_Q}{\sqrt{BB_N}\sqrt{W}} \cdot f\left(\frac{a}{W}\right) \tag{9}$$

where $P_Q$ is the provisional force, $W$ is the specimen width, $a$ is the crack length, $B$ is the specimen thickness, $B_N$ is the specimen thickness between the roots of the side grooves, in this study, $B = B_N$, $f$ is a function of the crack length ratio $a/W$.

A 5% secant method was used to determine $P_Q$ with the intent of defining the value of $K_{IC}$ at 2% or less crack extension. The 5% secant line with a slope equal to 95% of the initial elastic loading slope of the tangent line is constructed to determine $P_5$ [31]. The force-CMOD curves of 1/2 T specimens at different temperatures are shown in Fig. 9(a), the end point of the curves is the tensile fracture point. In this study, the force - CMOD curves at 173–293 K are smooth and deviate only slightly from linearity before reaching the maximum force ($P_{max}$), $P_Q = P_5$, while for specimens at 123 K, $P_Q = P_{max}$, corresponding to the Type I and Type III curves in the E399-20 standard, respectively. It can be seen that the proportion of plastic deformation work gradually decreases with decreasing temperature, reflecting that the specimen becomes more brittle with decreasing temperature. This is consistent with the fracture mechanism derived from the tensile tests. The Mode I provisional fracture toughness $K_Q$ for all 1/2 T specimens are listed in Table 5. When $K_Q$ meets the following two criteria, it is valid as $K_{IC}$

$$\text{Criterion 1}: \quad P_{max}/P_Q \leqslant 1.10 \tag{10}$$

$$\text{Criterion 2}: \quad 2.5(K_Q/\sigma_{YS})^2 \leqslant B, a \tag{11}$$

The average fracture toughness $K_{IC}$ for the LPBF Ti6Al4V specimens tested at different temperatures ranges from 54.36 ~ 64.87 MPa $\sqrt{m}$. After removing invalid $K_Q$ values, the average $K_{IC}$ of the specimens at 223 K and 123 K is 57.80 MPa $\sqrt{m}$ and 54.36 MPa $\sqrt{m}$, respectively. As shown in Fig. 9(b), the fracture toughness increases with increasing temperature. The fracture toughness at 293 K is about 10.51 MPa $\sqrt{m}$ higher than that at 123 K. The relationship between fracture toughness and temperature between 123 and 293 K was obtained by fitting the experimental results as follows, with $R^2 = 1$ (coefficient of determination, COD) for the fitted curve

$$K_{IC}(T) = 53.83 + 1.17T - 0.99T^2 + 0.35T^3 \tag{12}$$

The mechanical properties of LPBF alloys are strongly influenced by processing parameters and heat treatment processes. In these cases, studying the effect of temperature on fracture toughness allows the establishment of a simple fracture toughness-temperature correlation line. The result of plastic zone size in plane strain state obtained by Eq. (7) with $K_I = K_{IC}$ are also shown in Table 5. It is noted that the condition of SSY conditions ($r_p \ll r_k \approx 0.3a \sim 0.5a$) is satisfied at different temperatures in this study.

Fig. 10 shows the macroscopic fracture surface of LPBF Ti6Al4V specimens tested at different temperatures. The fracture surface is divided into the pre-crack region and the unstable crack propagation region. The fatigue pre-crack region has a relatively flat fracture surface where fatigue striations and small cracks can be observed. The macroscopic fracture surface of the unstable crack propagation region is relatively rough and covered with many dimples, indicating that ductile fracture is dominant. In addition, a large number of ravines oriented

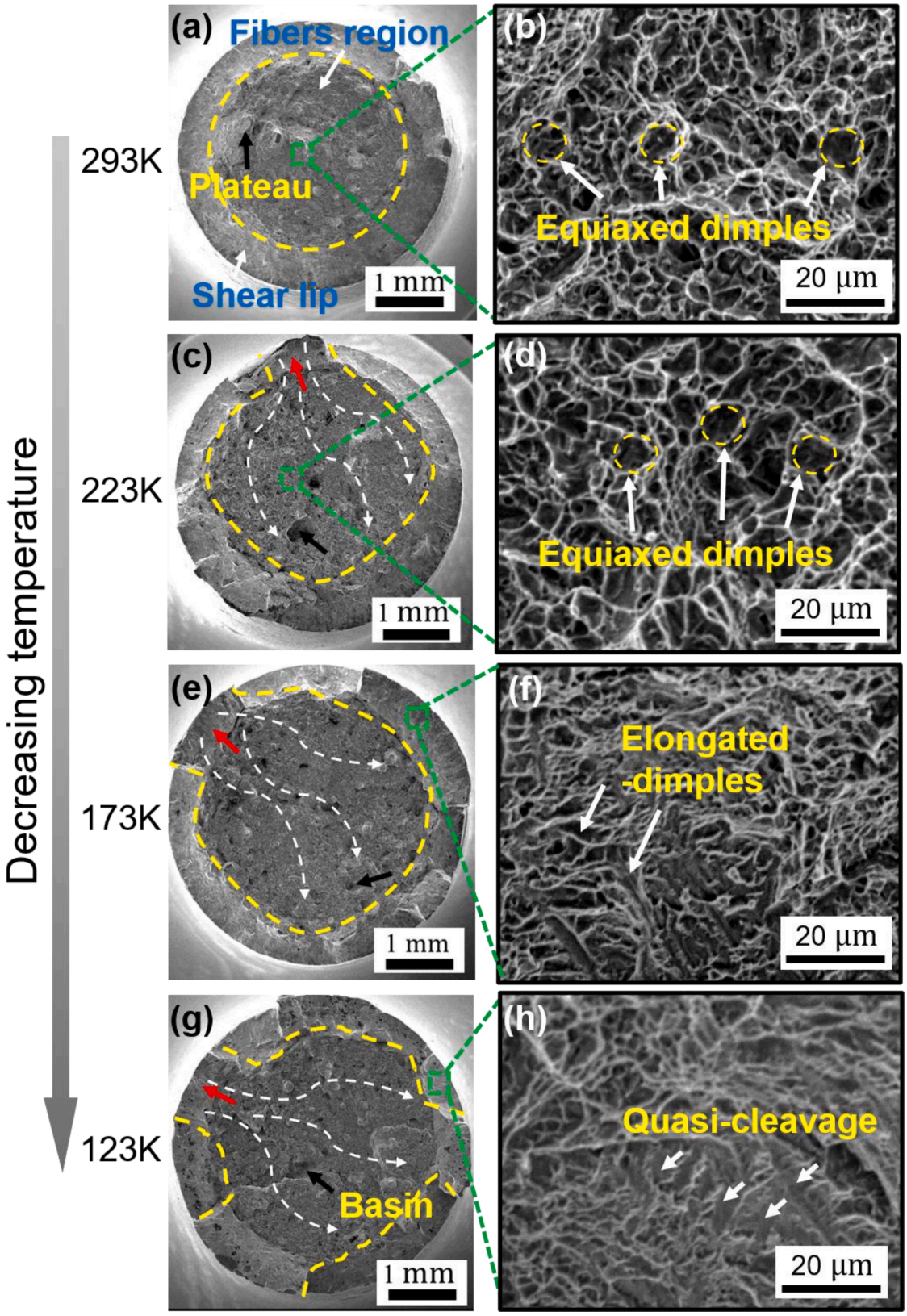


**Fig. 8.** Representative fracture surfaces of the tensile specimens: (a-b) 293 K, (c-d) 223 K, (e-f) 173 K, (g-h) 123 K. The red and black arrows in (b-d) indicate the defect responsible for the onset of fracture and the location of plateaus or basins, respectively.

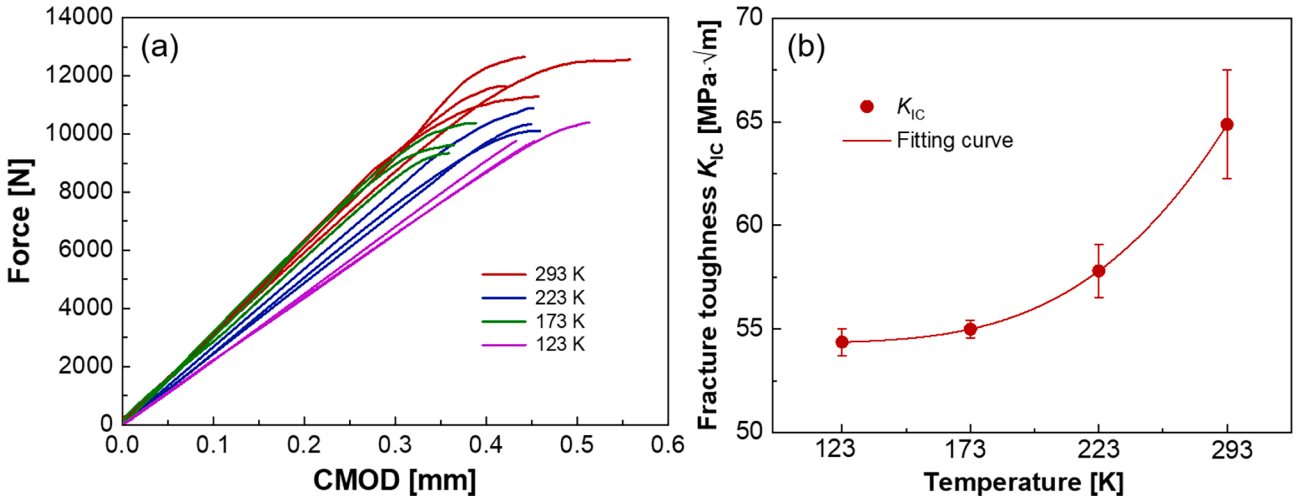


**Fig. 9.** The force-CMOD curves (a) and $K_{IC}$ values (b) of 1/2 T specimens at different temperatures.

**Table 5**
Fracture toughness of the tested specimens at different temperatures ($K_{IC}$ are the average values of the valid $K_Q$).

| Temperature [K] | Specimen number | $a/W$ [/] | $K_Q$ [MPa $\sqrt{m}$] | Criterion 1 | Criterion 2 | $K_{IC}$ [MPa $\sqrt{m}$] | $r_p$ [mm] |
|---|---|---|---|---|---|---|---|
| 293 | 1 | 0.55 | 61.70 | Pass | Pass | 64.87 | 0.14 |
| | 2 | 0.54 | 67.87 | Pass | Pass | | |
| | 3 | 0.55 | 64.01 | Pass | Pass | | |
| | 4 | 0.55 | 65.91 | Pass | Pass | | |
| 223 | 1 | 0.57 | 62.97 | Fail | Pass | 57.80 | 0.09 |
| | 2 | 0.55 | 56.89 | Pass | Pass | | |
| | 3 | 0.56 | 58.71 | Pass | Pass | | |
| 173 | 1 | 0.55 | 54.69 | Pass | Pass | 54.99 | 0.07 |
| | 2 | 0.58 | 58.60 | Pass | Pass | | |
| | 3 | 0.57 | 55.29 | Pass | Pass | | |
| 123 | 1 | 0.54 | 53.90 | Pass | Pass | 54.36 | 0.06 |
| | 2 | 0.55 | 60.41 | Fail | Pass | | |
| | 3 | 0.55 | 55.96 | Pass | Pass | | |

perpendicular to the build direction are clearly shown at the junction of the two regions are clearly shown. As the temperature decreases, the ravines become smaller and the fracture surface of the unstable crack propagation region becomes flatter. Usually, larger ravines and cone-shaped hills are caused by crack deflection during fracture and more energy is consumed [48], which may be a reason for the increased fracture toughness at higher temperature.

The main crack initiations observed in the LPBF Ti6Al4V alloy are: smooth facets with small cracks, LOF regions with un-melted powder and gas pores, as shown in Fig. 11. According to [49], defects are usually caused by insufficient energy (LOF defects) or excessive energy (gas pores) in the metallic LPBF process. In this study, both excessive energy and insufficient energy defects appeared in the fracture surfaces. $\alpha$-phase facet defects and microscopic small cracks are reported to be the source of crack initiation in traditionally manufactured Ti6Al4V alloy [50]. However, cracks in LPBF Ti6Al4V alloy can also originate from pores and LOF defects. That is, there are several competing fracture mechanisms in additively manufactured titanium alloys. The effect of defects on the fracture mechanism is significant, but defects in LPBF parts can be minimized by the use of high-quality powders, substrate preheating, optimization of process parameters and post heat treatment [51], resulting in improved fracture toughness. The final fracture toughness of additively manufactured Ti6Al4V alloy is ultimately determined by the number and location of defects within the specimen.

Fig. 12 illustrates the interaction between the crack path and the α colonies (prior β grains) characterized by EBSD of the sample at 173 K. The result shows that the primary crack propagates through the α colonies, namely translamellar propagation, and at the junction of the colonies, the crack will appear deflection. According to [52], the translamellar crack is strongly dependent on the active slip planes, while the interlamellar crack is closely related to the misorientation between the adjacent α-lamellas. In addition, the large orientation deviation between α lamellar will promote the deflection of cracks or lead to the alternating propagation of interlamellar cracks and translamelar cracks. Eventually, a serrated crack propagation path is formed. In general, the crack propagation path of the specimen is relatively flat, indicating that there is a small plastic deformation, which is consistent with the ductile–brittle mixed fracture mode of the low temperature tensile specimen shown in Fig. 8(c).

### 3.3.2. *Temperature effect on crack tip plastic zone*

A significant difference can be observed in the plastic deformation region of 1/2 T specimens at different temperatures, as shown in Fig. 10. To clearly get the size and shape of the CYPZ at different temperatures, finite element analysis (FEA) based on the elastic–plastic $J$-integral was used to characterize the crack tip filed. Von Mises stress distributions of the specimens at different temperatures are shown in Fig. 13. The gray area near the crack tip in the stress contour represents the plastic zone, where the von Mises stress exceeds the yield stress of the material. The size of the plastic zone is relatively small compared to the crack length and other characteristic dimensions. It can also be seen that the plastic yield occurs only near the crack tip position, and the plastic zone has a classic butterfly shape in the $XOY$ ($z = 0$) plane. As the temperature decreases, the maximum of the von Mises stress increases and the plastic zone of the crack tip gradually decreases. This may be the reason for the reduced fracture toughness of the material at low temperature, since the

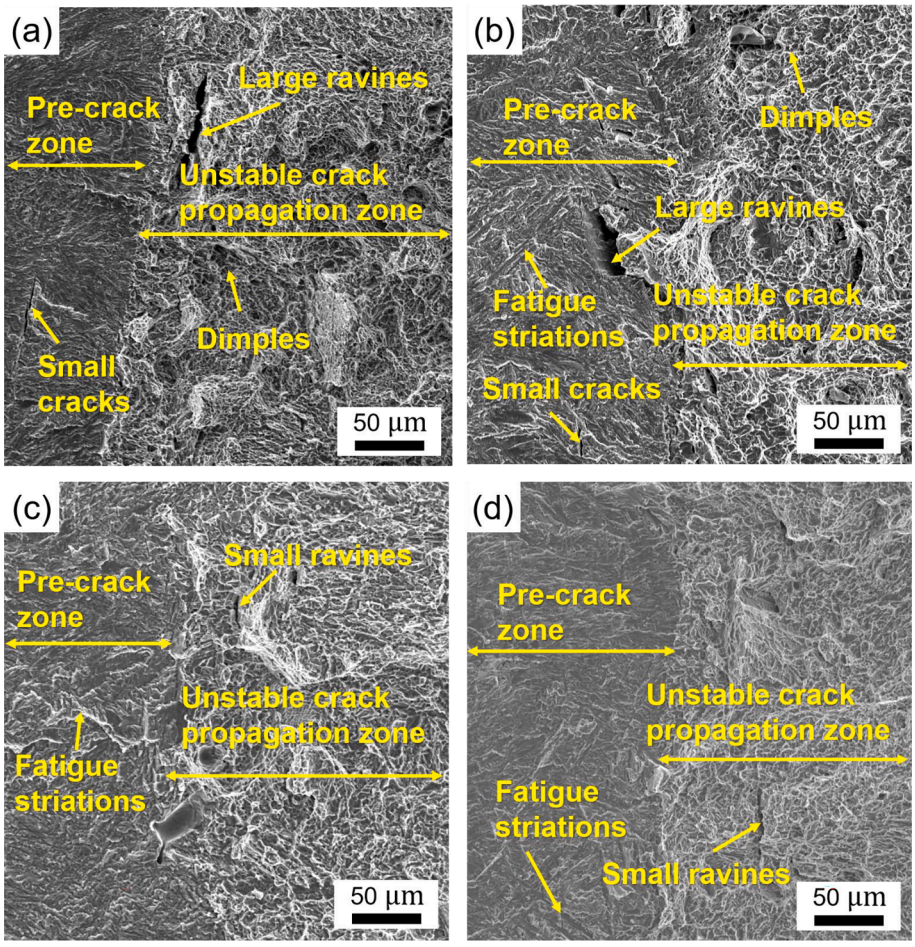


**Fig. 10.** Representative fracture surfaces of 1/2 T specimens at different temperatures: (a) 293 K, (b) 223 K, (c) 173 K, (d) 123 K.

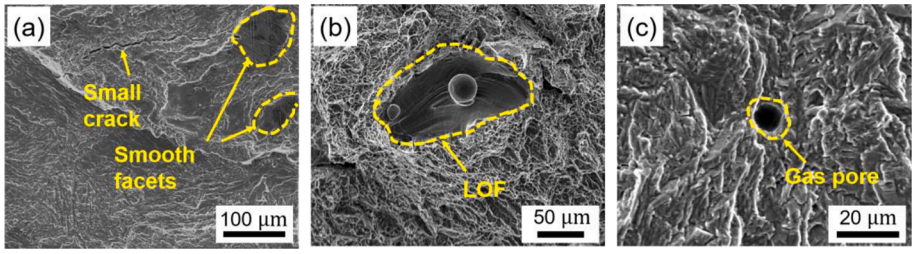


**Fig. 11.** Typical defects in the LPBF Ti6Al4V alloy: (a) smooth facets with small cracks, (b) LOF defects with un-melted powder particles, (c) gas pores.

plastic zone is the result of plastic deformation, which is accompanied by drastic energy consumption.

Fig. 14 shows the comparisons for the CTPZ contour lines in the mid-symmetry plane between the results obtained by FEA and those predicted by the theoretical solutions Eqs. (2) and (3) when the horizontal displacement constraint reaches to the limit of 0.3 mm at different temperatures. In the mid-symmetry plane, the plane strain plastic zone is much smaller than the plane stress plastic zone, the former condition suppresses yielding, resulting in a smaller plastic zone for a given load value. The area of the plastic zone decreases with the decreasing of temperature. The FEA plastic zone area of the specimen at 123 K is only about one-third of that at 293 K. The smaller the plastic zone is, the specimen at low temperature is less likely to yield and more prone to brittle fracture than the specimen at room temperature. This explains the increase in tensile yield strength at low temperature, and is consistent with the mixed ductile–brittle fracture mode exhibited at low temperature. The plastic zone calculated by FEA is closer to the plane strain plastic zone. It indicates that our finite element simulation satisfies the plane strain condition, which is consistent with the results of most specimens meeting the $K_{IC}$ validity criteria, and also proves the reliability of the FEA results in this study.

Fig. 15(a) shows the distributions of the $J$-integral in the mid-symmetry plane. The $J$-integral increases monotonically with increasing loading displacement. It is interesting to notice that the $J$-integral of the specimen at 173 K is larger than that of 123 K for the same load. It can be found that the variation of $J$-integral with temperature follows the same trend as the variation of Young's modulus with temperature. A subroutine was developed to accurately calculate the volume of the plastic zone ($V_p$) near the crack tip, as shown in Fig. 15(b). When the loading displacement is less than 0.1 mm, the specimen does not undergo plastic deformation, and the $V_p$ is 0. For the same load displacement, the $V_p$ decreases with the decreasing of temperature.

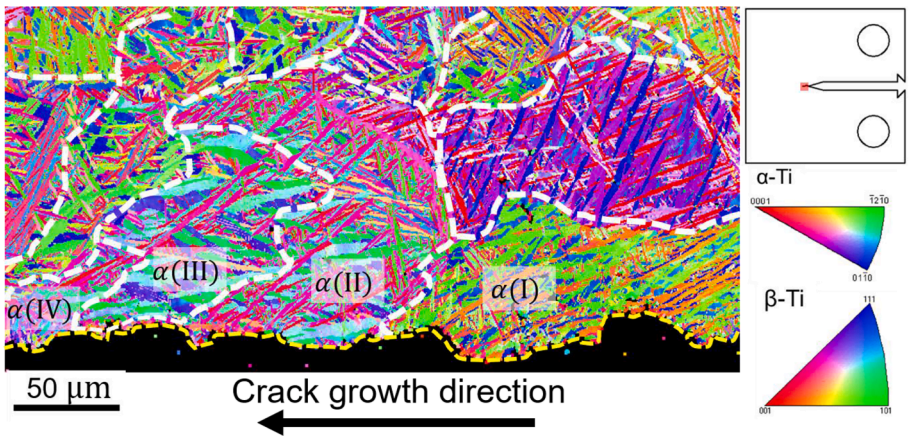


**Fig. 12.** EBSD IPF map of the crack path for a 173 K sample. The white dotted lines indicate α colonies and the yellow dotted lines mark the crack path profile.

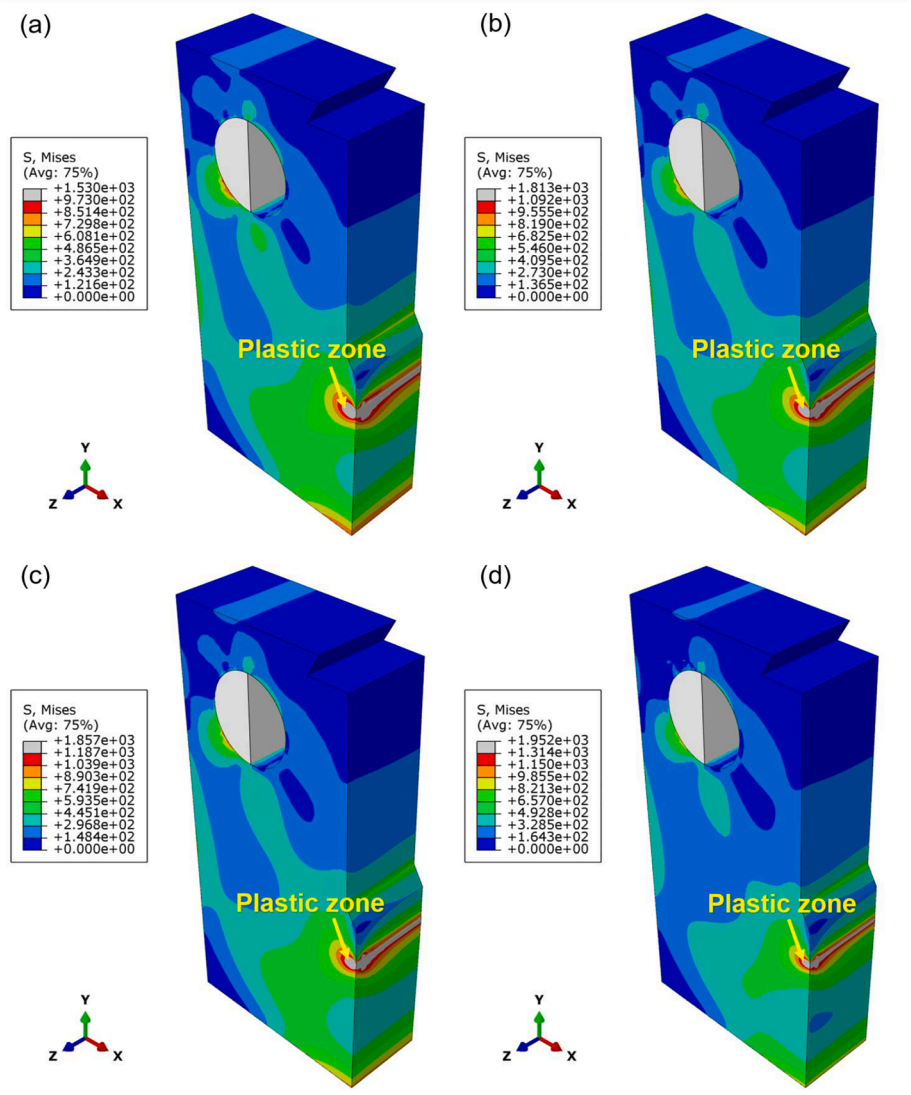


**Fig. 13.** Von Mises stress distributions of 1/2 T specimens at different temperatures: (a) 293 K, (b) 223 K, (c) 173 K, (d) 123 K.

Researchers have found that both high-purity Ti and Ti-5at%Al have significantly harder dislocation motion at liquid nitrogen temperatures (77 K) than at room temperature. At low temperatures, the dislocation motion of high-purity Ti is even more difficult than that of Ti-5at%Al [53]. For LPBF Ti6Al4V alloy, the dislocation motion can also be retarded at low temperature, which resulting in the reduction of plastic energy dissipation. The macroscopic manifestation is that the fracture toughness decreases with the decreasing of temperature. In some

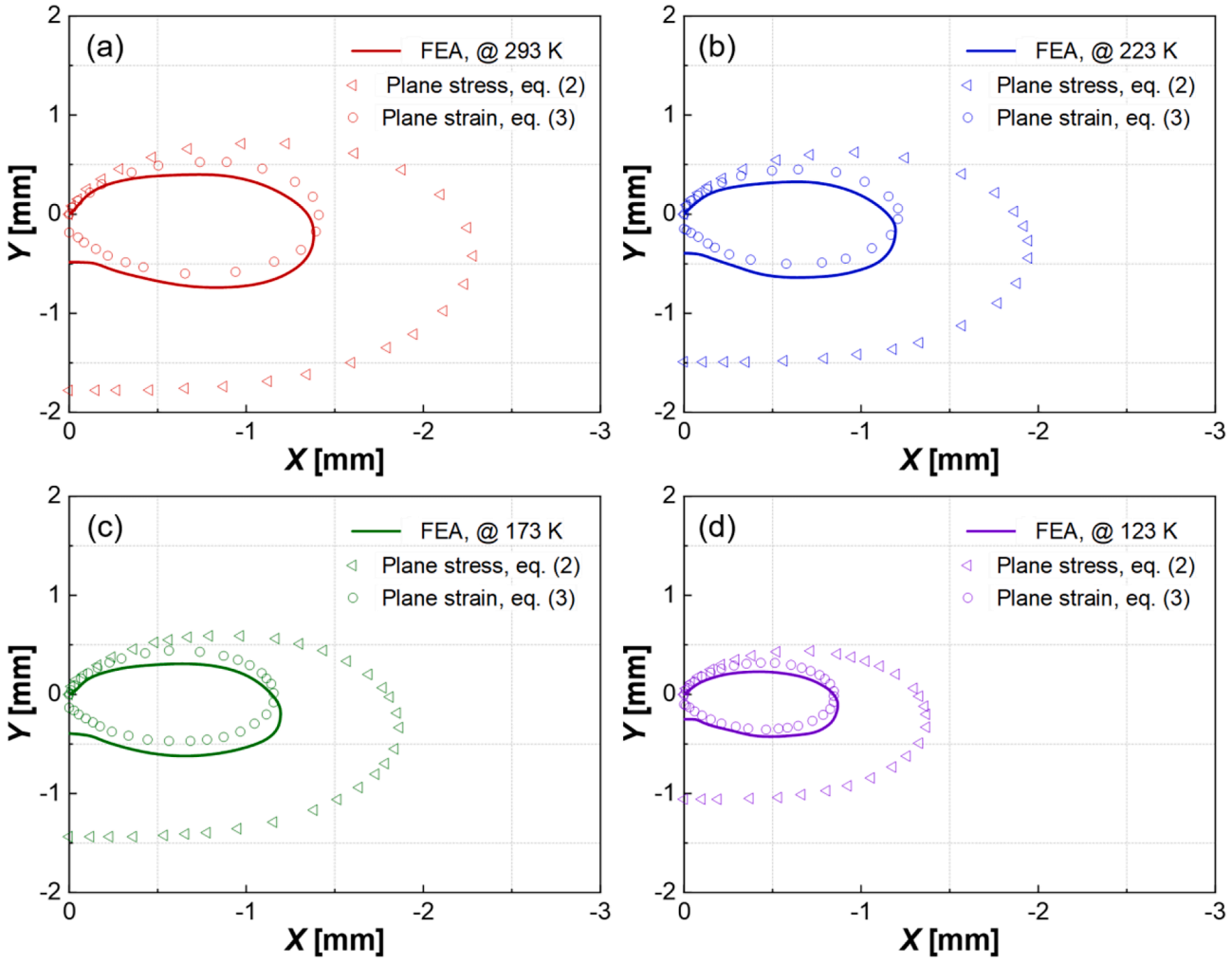


**Fig. 14.** Results predicted by theoretical solutions Eqs. (2) and (3) compared with FEA for the CTPZ contour lines in the mid-symmetry plane ($z = 0$) of 1/2 T specimens at various temperatures.

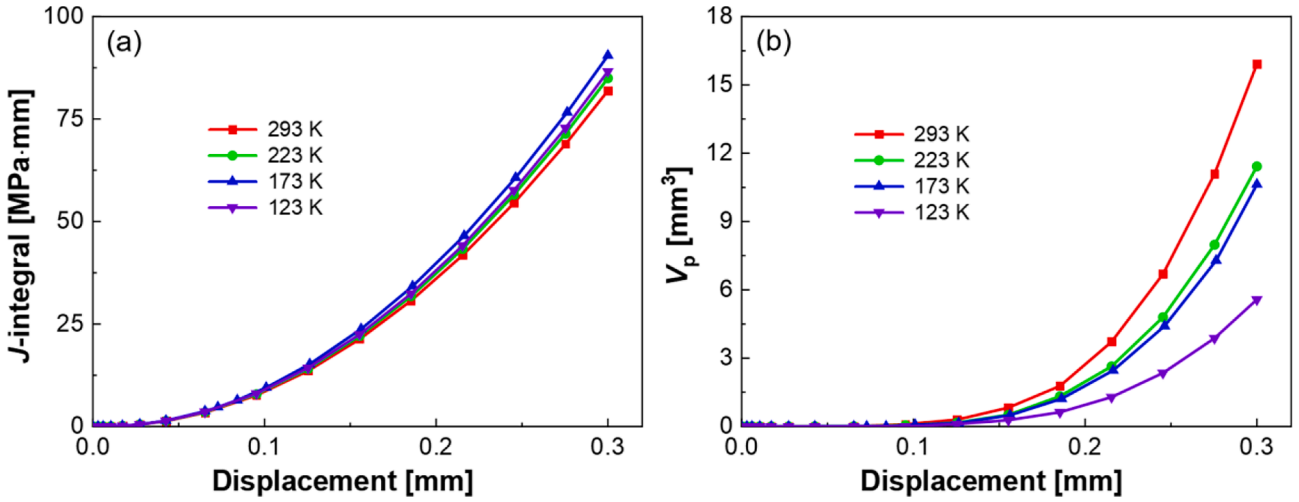


**Fig. 15.** The distribution of the $J$-integral in the mid-symmetry plane (a) and the volume of the plastic zone near the crack tip (b) at different temperatures.

extreme service environments, materials with properties to resist cryogenic temperatures and intense vibration are required [54]. In the future, we could explore fracture and fatigue life studies of LPBF Ti6Al4V at low temperatures while taking into account defect size and location.

The relationships between $J$-integral and $V_p$ for specimens at different temperatures are shown in Fig. 16. It can be seen that the variation of $V_p$ with $J$-integral is similar to the variation of $K_{IC}$ with

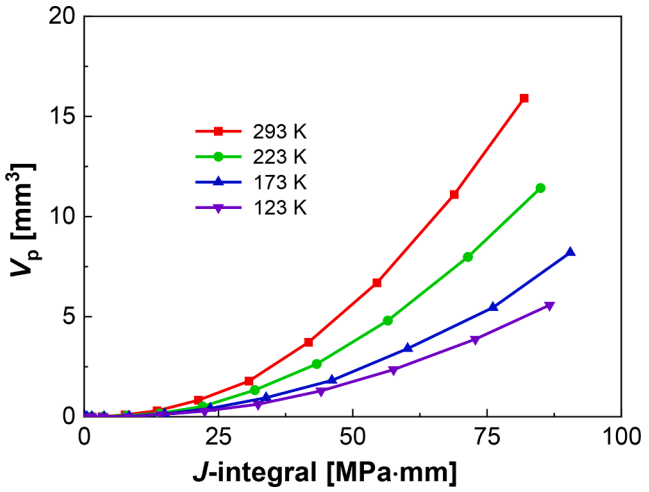


**Fig. 16.** Relationship between $J$-integral and $V_p$ for specimens at different temperatures.

temperature. The $J$-integral is affected by both loading and material properties. In the future, it may be possible to find the unified relationship between $V_p$ and $J$-integral at different temperatures, so that the fracture toughness of materials at different temperatures can be predicted by FEA. However, such an attempt would require a large number of experiments with FEA results to ensure reliability.

## 4. Conclusions

In this paper, effects of temperature on the tensile and fracture performance of the LPBF Ti6Al4V alloy were investigated. The microstructure anisotropy and fracture surfaces of specimens at different temperatures were analyzed. The following conclusions are drawn:

(1) The tensile strength obviously increases with decreasing temperature. The yield strength of the specimen at 123 K is 35% higher than that at 293 K, and the corresponding fracture elongation decreases by only 2.9%. The fracture mode changes from ductile fracture at room temperature to a mixed mode at low temperature.
(2) A correlation of fracture toughness and temperature between 123 and 293 K was obtained. The fracture toughness of the specimen at 123 K is 16.2% lower than that at 293 K. Smooth facets with small cracks, LOF regions and gas pores can form the crack initiation in LPBF Ti6Al4V alloy.
(3) The crack tip plastic zone size decreases with the decreasing of temperature. This may be because the dislocation motion is retarded at low temperature, resulting in the reduction of plastic energy dissipation. The variation of plastic zone is consistent with that of fracture toughness with temperature.
(4) The LPBF Ti6Al4V alloy exhibits strong microstructural anisotropy. The texture strength of the samples differs by nearly 50% in the direction parallel to and perpendicular to the build direction. This is determined by the micro- and meso-structures of the LPBF Ti6Al4V alloy, and stress relieving annealing cannot completely eliminate the anisotropy.

## CRediT authorship contribution statement

**Yingmeng Xiao:** Investigation, Methodology, Software, Formal analysis, Data curation, Writing – original draft, Writing – review & editing. **Guian Qian:** Conceptualization, Methodology, Supervision, Writing – review & editing. **Jingyu Sun:** Conceptualization, Writing – review & editing. **Filippo Berto:** Writing – review & editing. **Jose A.F. Correia:** Writing – review & editing. **Youshi Hong:** Writing – review & editing.

## Declaration of Competing Interest

The authors declare that they have no known competing financial interests or personal relationships that could have appeared to influence the work reported in this paper.

## Data availability

Data will be made available on request.

## Acknowledgements

This work was funded by the National Natural Science Foundation of China (No. 11932020, 12072345), and National Science and Technology Major Project (J2019-VI-0012-0126) and Science Center for Gas Turbine Project (P2022-B-III-008-001).

## References

[1] J.H. Martin, B.D. Yahata, J.M. Hundley, J.A. Mayer, T.A. Schaedler, T.M. Pollock, 3D printing of high-strength aluminium alloys, Nature 549 (2017) 365–369.
[2] Z. Snow, R. Martukanitz, S. Joshi, On the development of powder spreadability metrics and feedstock requirements for powder bed fusion additive manufacturing, Addit. Manuf. 28 (2019) 78–86.
[3] I. Gibson, D. Rosen, B. Stucker, M. Khorasani, Additive Manufacturing Technology, in, Springer Nature Switzerland AG, Switzerland, 2021.
[4] W.E. Frazier, Metal Additive Manufacturing: A Review, J. Mater. Eng. Perform. 23 (2014) 1917–1928.
[5] J.J. Lewandowski, M. Seifi, Metal Additive Manufacturing: A Review of Mechanical Properties, Annu. Rev. Mat. Res. 46 (2016) 151–186.
[6] L. Du, G. Qian, L. Zheng, Y. Hong, Influence of processing parameters of selective laser melting on high-cycle and very-high-cycle fatigue behaviour of Ti-6Al-4V, Fatigue Fract. Eng. Mater. Struct. 44 (2020) 240–256.
[7] N.T. Aboulkhair, N.M. Everitt, I. Ashcroft, C. Tuck, Reducing porosity in AlSi10Mg parts processed by selective laser melting, Addit. Manuf. 1–4 (2014) 77–86.
[8] G. Kasperovich, J. Hausmann, Improvement of fatigue resistance and ductility of TiAl6V4 processed by selective laser melting, J. Mater. Process. Technol. 220 (2015) 202–214.
[9] G.M. Ter Haar, T.H. Becker, Selective Laser Melting Produced Ti-6Al-4V: Post-Process Heat Treatments to Achieve Superior Tensile Properties. Materials (Basel) 2018; 11.
[10] U. Tradowsky, J. White, R.M. Ward, N. Read, W. Reimers, M.M. Attallah, Selective laser melting of AlSi10Mg: Influence of post-processing on the microstructural and tensile properties development, Mater. Des. 105 (2016) 212–222.
[11] S. Leuders, M. Thöne, A. Riemer, T. Niendorf, T. Tröster, H.A. Richard, H.J. Maier, On the mechanical behaviour of titanium alloy TiAl6V4 manufactured by selective laser melting: Fatigue resistance and crack growth performance, Int. J. Fatigue 48 (2013) 300–307.
[12] T.H. Becker, P. Kumar, U. Ramamurty, Fracture and fatigue in additively manufactured metals, Acta Mater. 219 (2021).
[13] L. Zhu, N. Li, P.R.N. Childs, Light-weighting in aerospace component and system design, Propul. Power Res. 7 (2018) 103–119.
[14] D.D. Gu, W. Meiners, K. Wissenbach, R. Poprawe, Laser additive manufacturing of metallic components: materials, processes and mechanisms, Int. Mater. Rev. 57 (2013) 133–164.
[15] L. Thijs, F. Verhaeghe, T. Craeghs, J.V. Humbeeck, J.-P. Kruth, A study of the microstructural evolution during selective laser melting of Ti–6Al–4V, Acta Mater. 58 (2010) 3303–3312.
[16] P. Kumar, O. Prakash, U. Ramamurty, Micro-and meso-structures and their influence on mechanical properties of selectively laser melted Ti-6Al-4V, Acta Mater. 154 (2018) 246–260.
[17] J. Yang, H. Yu, J. Yin, M. Gao, Z. Wang, X. Zeng, Formation and control of martensite in Ti-6Al-4V alloy produced by selective laser melting, Mater. Des. 108 (2016) 308–318.
[18] L. Thijs, M.L. Montero Sistiaga, R. Wauthle, Q. Xie, J.-P. Kruth, J., Van Humbeeck, Strong morphological and crystallographic texture and resulting yield strength anisotropy in selective laser melted tantalum, Acta Mater. 61 (2013) 4657–4668.
[19] S.L. Lu, Z.J. Zhang, R. Liu, X.H. Zhou, X.G. Wang, B.N. Zhang, X.M. Zhao, J. Eckert, Z.F. Zhang, Optimal tensile properties of laser powder bed fusion hereditary basket-weave microstructure in additive manufactured Ti6Al4V, Addit. Manuf. 59 (2022).
[20] P. Andresen, B. Antolovich, ASM Handbook, in: Fatigue and Fracture, ASM International, vol. 19, 1996, p. 1057.
[21] F. Bartolomeu, M. Gasik, F.S. Silva, G. Miranda, Mechanical Properties of Ti6Al4V Fabricated by Laser Powder Bed Fusion: A Review Focused on the Processing and Microstructural Parameters Influence on the Final Properties. Metals 2022;12.

[22] V. Cain, L. Thijs, J. Van Humbeeck, B. Van Hooreweder, R. Knutsen, Crack propagation and fracture toughness of Ti6Al4V alloy produced by selective laser melting, Addit. Manuf. 5 (2015) 68–76.
[23] S. Cao, Y. Zou, C.V.S. Lim, X. Wu, Review of laser powder bed fusion (LPBF) fabricated Ti-6Al-4V: process, post-process treatment, microstructure, and property. Light: Advanced Manufacturing 2021;2.
[24] P. Kumar, U. Ramamurty, Microstructural optimization through heat treatment for enhancing the fracture toughness and fatigue crack growth resistance of selective laser melted Ti-6Al-4V alloy, Acta Mater. 169 (2019) 45–59.
[25] M.R. Khosravani, F. Berto, M.R. Ayatollahi, T. Reinicke, Fracture behavior of additively manufactured components: A review, Theor. Appl. Fract. Mech. 109 (2020).
[26] G. Singh, U. Ramamurty, Reprint: Boron modified titanium alloys, Prog. Mater Sci. 120 (2021).
[27] T. Yuri, Y. Ono, T. Ogata, Notch effects on high-cycle fatigue properties of Ti–6Al–4V ELI alloy at cryogenic temperatures, Cryogenics 46 (2006) 30–36.
[28] G. Singh, G. Bajargan, R. Datta, U. Ramamurty, Deformation and strength of Ti–6Al–4V alloyed with B at cryogenic temperatures, Mater. Sci. Eng. A 611 (2014) 45–57.
[29] J.R. Rice, A Path Independent Integral and the Approximate Analysis of Strain Concentration by Notches and Cracks, J. Appl. Mech. 35 (1968) 379–386.
[30] B. Zhang, Y. Li, Q. Bai, Defect Formation Mechanisms in Selective Laser Melting: A Review, Chin. J. Mech. Eng. 30 (2017) 515–527.
[31] W. Conshohocken, Standard Test Method for Linear-Elastic Plane-Strain Fracture Toughness of Metallic Materials, in, PA, 2020.
[32] T.L. Anderson, Fracture Mechanics Fundamentals And Applications 3rd Ed, in, CRC Press, New York, 1995.
[33] G.R. Irwin, Analysis of Stresses and Strains Near the End of a Crack Traversing a Plate, J. Mech. Phys. Solids 24 (1957) 361–364.
[34] J.W. Hutchinson, Singular behaviour at the end of a tensile crack in a hardening material, J. Mech. Phys. Solids 16 (1968) 13–31.
[35] J.R. Rice, G.F. Rosengren, Plane Strain Deformation near a Crack Tip in a Power-Law Hardening Material, J. Mech. Phys. Solids 16 (1968) 1 -+.
[36] X.-K. Zhu, J.A. Joyce, Review of fracture toughness (G, K, J, CTOD, CTOA) testing and standardization, Eng. Fract. Mech. 85 (2012) 1–46.
[37] S. Diiorio, L. Briottet, E. Rauch, D. Guichard, Plastic deformation, damage and rupture of PM Ti–6Al–4V at 20K under monotonic loading, Acta Mater. 55 (2007) 105–118.
[38] A.A. Wells, Application of fracture mechanics at and beyond general yielding. British Welding Research Assoc Rep M13/63 1963;10:563-570.
[39] H. Xin, J.A.F.O. Correia, M. Veljkovic, Three-dimensional fatigue crack propagation simulation using extended finite element methods for steel grades S355 and S690 considering mean stress effects, Eng. Struct. 227 (2021).
[40] W. Sun, Y.e. Ma, W. Huang, W. Zhang, X. Qian, Effects of build direction on tensile and fatigue performance of selective laser melting Ti6Al4V titanium alloy, Int. J. Fatigue 2020; 130.
[41] G. Qian, Y. Li, D.S. Paolino, A. Tridello, F. Berto, Y. Hong, Very-high-cycle fatigue behavior of Ti-6Al-4V manufactured by selective laser melting: Effect of build orientation, Int. J. Fatigue 136 (2020).
[42] Y. Kok, X.P. Tan, P. Wang, M.L.S. Nai, N.H. Loh, E. Liu, S.B. Tor, Anisotropy and heterogeneity of microstructure and mechanical properties in metal additive manufacturing: A critical review, Mater. Des. 139 (2018) 565–586.
[43] N. Sanaei, A. Fatemi, Defects in additive manufactured metals and their effect on fatigue performance: A state-of-the-art review, Prog. Mater Sci. 117 (2021).
[44] R. Sołtysiak, J. Małecka, The analysis of cyclic properties of Ti-6Al-4V titanium alloy at room and liquid nitrogen temperature, Mater. Sci. Eng. A 734 (2018) 476–484.
[45] A. Soltani-Tehrani, M. Habibnejad-Korayem, S. Shao, M. Haghshenas, N. Shamsaei, Ti-6Al-4V powder characteristics in laser powder bed fusion: The effect on tensile and fatigue behavior, Addit. Manuf. (2022) 51.
[46] M. Simonelli, Y.Y. Tse, C. Tuck, Effect of the build orientation on the mechanical properties and fracture modes of SLM Ti–6Al–4V, Mater. Sci. Eng. A 616 (2014) 1–11.
[47] Y. Lu, Y.H. Zhang, E. Ma, W.Z. Han, Relative mobility of screw versus edge dislocations controls the ductile-to-brittle transition in metals, Proc. Natl. Acad. Sci. U S A 118 (2021).
[48] H. Wang, Q. Zhao, S. Xin, Y. Zhao, W. Zhou, W. Zeng, Microstructural morphology effects on fracture toughness and crack growth behaviors in a high strength titanium alloy, Mater. Sci. Eng. A 821 (2021).
[49] G. Kasperovich, J. Haubrich, J. Gussone, G. Requena, Correlation between porosity and processing parameters in TiAl6V4 produced by selective laser melting, Mater. Des. 105 (2016) 160–170.
[50] S. Tammas-Williams, P.J. Withers, I. Todd, P.B. Prangnell, The Influence of Porosity on Fatigue Crack Initiation in Additively Manufactured Titanium Components, Sci. Rep. 7 (2017) 7308.
[51] W.J. Sames, F.A. List, S. Pannala, R.R. Dehoff, S.S. Babu, The metallurgy and processing science of metal additive manufacturing, Int. Mater. Rev. 61 (2016) 315–360.
[52] S. Birosca, J.Y. Buffiere, F.A. Garcia-Pastor, M. Karadge, L. Babout, M. Preuss, Three-dimensional characterization of fatigue cracks in Ti-6246 using X-ray tomography and electron backscatter diffraction, Acta Mater. 57 (2009) 5834–5847.
[53] B. Zhao, P. Huang, L. Zhang, S. Li, Z. Zhang, Q. Yu, Temperature Effect on Stacking Fault Energy and Deformation Mechanisms in Titanium and Titanium-aluminium Alloy, Sci. Rep. 10 (2020) 3086.
[54] D.-K. Chang, Q.-Q. Wang, H. Chen, X.-C. Zhang, J.-F. Wen, S.-T. Tu, Effects of defect size and location on high cycle fatigue life of a maraging stainless steel at ambient and cryogenic temperatures, Int. J. Fatigue 161 (2022).